

The source-sample stage of the new two-dimensional angular correlation of annihilation radiation spectrometer at Technische Universität München

Hubert Ceeh, Josef Andreas Weber, Michael Leitner, Peter Böni, and Christoph Hugenschmidt

Citation: *Rev. Sci. Instrum.* **84**, 043905 (2013); doi: 10.1063/1.4801454

View online: <http://dx.doi.org/10.1063/1.4801454>

View Table of Contents: <http://rsi.aip.org/resource/1/RSINAK/v84/i4>

Published by the [American Institute of Physics](http://www.aip.org/).

Additional information on *Rev. Sci. Instrum.*

Journal Homepage: <http://rsi.aip.org>

Journal Information: http://rsi.aip.org/about/about_the_journal

Top downloads: http://rsi.aip.org/features/most_downloaded

Information for Authors: <http://rsi.aip.org/authors>

ADVERTISEMENT

physicstoday

Comment on any
Physics Today article.

Physics Today / Volume 63 / Issue 7 / July 2012
Previous Article | Next Article

Measured energy in Japan
David von Seggern
(dvseg@seismo.unr.edu) University of Nevada
July 2012, page 10
DIGITAL OBJECT IDENTIFIER
<http://dx.doi.org/10.1063/PT.3.1619>
The article by Thorne Lay and Hiroo Kanamori (2012) is an excellent review of the energy released by the 2011 Tohoku earthquake and tsunami. It is estimated that the earthquake released approximately five times as much energy as the 1964 Chilean earthquake. The authors also mention that the 1964 Chilean earthquake had still more energy by a factor of about 3, or 15 times as much energy as the 1964 Chilean earthquake. I believe the authors used the relation for seismic energy release rather than total strain energy release. The seismic energy underestimates the total strain energy release by a variable that depends on friction on the fault plane. Accounting for total strain energy release would increase the earthquake energy number by orders of magnitude. Despite the catastrophic damage potential of nuclear bombs, the forces of nature occasionally unleash much larger energy releases. Although the nuclear bombs are under our control, earthquakes, volcanic eruptions, and extreme weather events are not. However, by judicious preparation and avoidance measures, humans can significantly diminish the damage of natural events.

Comment on this article
By the act of hitting a ball with a bat, one calculates the force energy to deliver the ball to its new location, but one must also take into account that the ball extended its energy to the entire team. Therefore the parameters of the damage extend into the future when the received energy to that pushed upon, later becomes released in a new event. Perhaps calculations of one added that in while another's calculations did not. E.M.C.
Written by Edgar Mocarvill, 14 July 2012 19:59

The source-sample stage of the new two-dimensional angular correlation of annihilation radiation spectrometer at Technische Universität München

Hubert Ceeh,^{1,a)} Josef Andreas Weber,¹ Michael Leitner,² Peter Böni,¹ and Christoph Hugenschmidt^{1,2}

¹Technische Universität München, Lehrstuhl E21, James-Franck Straße, 85747 Garching, Germany

²FRM II, Technische Universität München, Lichtenbergstraße 1, 85747 Garching, Germany

(Received 15 October 2012; accepted 25 March 2013; published online 18 April 2013)

Angular correlation of annihilation radiation (ACAR) is a well established technique for the investigation of the electronic structure. A major limitation of ACAR studies is the available positron flux at a small spot on the sample. For this reason, the focus of this work is put on the discussion of a newly developed source-sample stage of the new 2D-ACAR spectrometer at Technische Universität München which uses an optimized static magnetic field configuration to guide the positrons onto the sample. The achieved spot diameter is $d_{\text{FWHM}} = 5.4$ mm, with a high efficiency over the whole energy spectrum of the ^{22}Na positron source. The implications of the performance of the source-sample stage are discussed with regard to 2D-ACAR measurements of single crystalline α -quartz, which serves as a model system for the determination of the total resolution. A value of (1.53×1.64) mrad² FWHM was achieved at room temperature. © 2013 AIP Publishing LLC. [<http://dx.doi.org/10.1063/1.4801454>]

I. INTRODUCTION

Almost all properties of materials are defined by their electronic structure. For a metal, the most important characteristic is the boundary between occupied and unoccupied states in reciprocal space, which is called the Fermi surface. In fact, a wide range of phenomena can be explained in terms of its shape and topology and have been investigated by 2D-ACAR (angular correlation of annihilation radiation). The traditional experimental methods for studying the Fermi surface rely on quantum-oscillations, such as the de Haas-van Alphen effect, which record the response of the sample magnetisation to high external magnetic fields, however, quantum-oscillatory methods usually require low measurement temperatures and highly ordered systems. The method of Angle-Resolved Photo-Emission Spectroscopy (ARPES), is only sensitive to surfaces, i.e., to the topmost few atomic layers.¹⁶ Both methods, quantum-oscillations and ARPES, therefore cannot serve as a general-purpose tool at finite temperatures for studying effects such as bulk phase transitions.

ACAR from positron-electron annihilation in matter is free from limitations such as low temperatures and high magnetic fields, therefore temperature dependent studies of the electronic structure are feasible. ACAR works as follows: in ACAR experiments, the deviation from the anti-parallel propagation directions of the two annihilation quanta is measured in coincidence. Using spatially resolved detectors, two-dimensional projections of the electron momentum density can be measured, which are used to reconstruct the three-dimensional electron momentum density of the sample. Among the numerous examples for 2D-ACAR investigations of the electronic structure found in the literature we compiled a short list of references related to major fields of

solid-state physics. For example, the relation of magnetic ordering to features of the Fermi surface has been studied in rare earths and their compounds.¹⁻³ Also, anisotropies in the Fermi surface, so called Fermi surface nesting, which cause the formation of a spin- or charge-density have been observed by 2D-ACAR.⁴⁻⁶ Using a ^{22}Na positron source allows for the spin-resolved determination of the electronic structure, i.e., the Fermi surface, respective investigations were undertaken in ferromagnetic⁷ and half-metallic⁸ materials. In addition, 2D-ACAR has been used to gain insight to many other phenomena linked to Fermi surface nesting, such as the ferromagnetic shape-memory effect⁹ and superconductivity.¹⁰⁻¹² Furthermore, positrons are uniquely well suited to probe the Fermi surface^{13,14} and compositional or structural changes¹⁵ of nano scale precipitates. This short list makes no claim to completeness, however, it shall give a rough overview of the problems that can be addressed with 2D-ACAR.

For 2D-ACAR, the limitations lie in the achievable count rate and resolution. Therefore, the goal is to guide, by means of a magnetic field, as many of the emitted positrons (from a radioactive source) as possible with a wide spectrum of energies onto a sample within a small spot as small as possible since this defines the achievable momentum resolution.

Here we present an overview of the recently completed 2D-ACAR spectrometer at the Technische Universität München (TUM) and the design of a source-sample stage optimized for efficient positron transport, as well as the measured performance.

II. LAYOUT OF THE NEW 2D-ACAR SPECTROMETER

A. Overview

The 2D-ACAR spectrometer consists of two main components, the source-sample chamber including the sample environment, and the detector assembly consisting of two

^{a)}Electronic mail: hubert.cee@frm2.tum.de

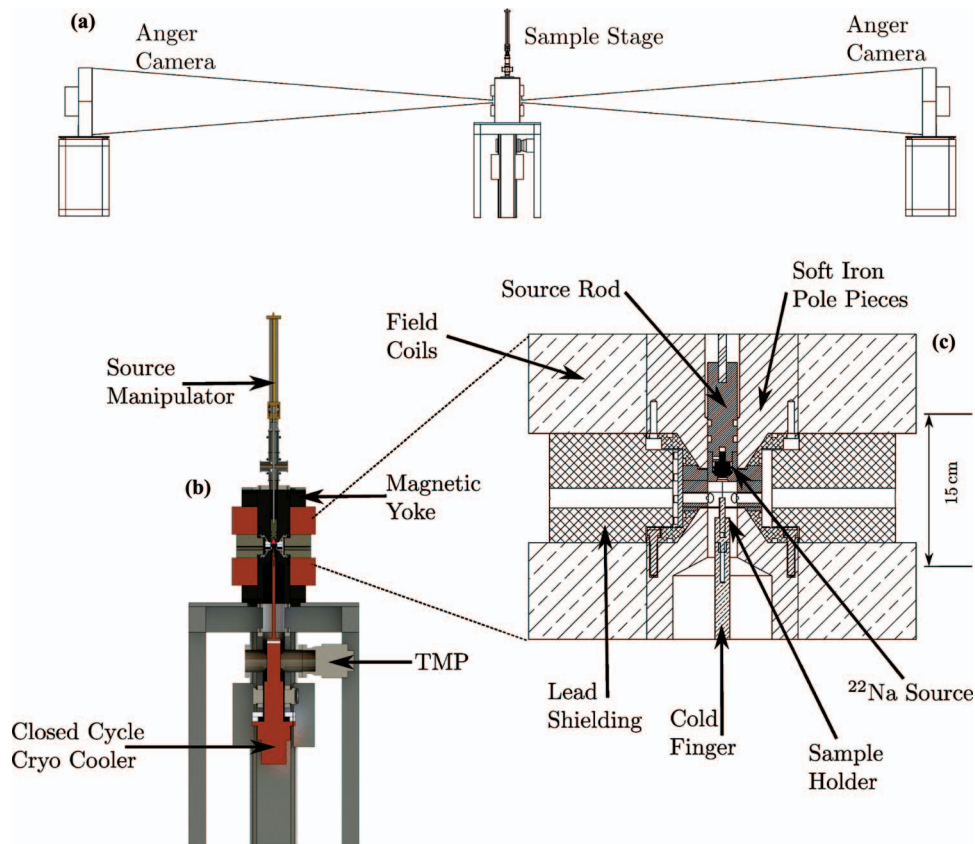


FIG. 1. Schematic overview of the ACAR spectrometer. (a) Total view of the spectrometer, including detectors. The baseline of the Anger cameras is 16.5 m in order to achieve the desired angular resolution. (b) Cut-view of the central assembly. The cold finger of the cryostat is fed into the sample chamber from below. (c) Detailed cut-view of the source-sample chamber with the custom-built pole piece assembly. Sample and source are positioned symmetrical with respect to the pole pieces.

Anger-type γ -cameras,¹⁷ which were obtained from the positron group of Bristol university. A total view of the spectrometer is given in Figure 1(a).

B. Detector system

The Anger cameras consist of a large NaI:Tl scintillation crystal with a thickness of 10.5 mm coupled to 61 photomultiplier tubes. The active area is collimated to a diameter of 41.5 cm by a lead ring, in order to exclude the part of the detector where the position response becomes nonlinear due to the discontinuity in the light collection efficiency at the borders of the crystal. The position information is obtained from the center of mass of the light signal produced in the scintillator. The individual photomultiplier signals are summed up in an analogue weighting resistor network in horizontal and vertical direction and are then divided by the integral signal of all photomultiplier tubes. The resulting x - and y -signals are shaped and amplified before they are fed into the data acquisition system. Parallel to the determination of the center of mass a logic analyzer circuit checks if the integral signal, which corresponds to the energy of the event, lies within a window of about ± 35 keV around the 511 keV photo peak. If this is the case a logic signal is produced and is fed to an analogue coincidence unit. If both cameras produce an appropriate analyzer signal, the data acquisition is triggered by the coincidence unit.

The two Anger cameras are positioned symmetrically at a distance of 8.25 m to the source-sample chamber. As the typical angular deviation lies in the order of milliradians, a long baseline is needed to resolve such small angles. The angular resolution is limited due to the finite spatial resolution of ≈ 3.5 mm of the Anger cameras. By increasing the baseline the angular resolution could be improved at the expense of the count rate, which decreases quadratically with the length of the baseline. An asymmetric spacing of the detectors relative to the sample chamber would result in a momentum sampling function with flat center,¹⁸ which can be beneficial for the data treatment. However, the attainable resolution is always limited by the detector with the shorter distance to the sample. Therefore, we chose a symmetric spacing in order to achieve the maximum resolution given the limited space in the experimental hall. To avoid errors by a transverse pitch and yaw of the Anger cameras their respective axes are aligned collinear with an accuracy of ± 1 mm using a laser positioning system in combination with a theodolite. Minor misalignment of the detectors can also be corrected offline in the data, since the positions for each coincident event on the detectors are stored in list-mode. By this it is also possible to correct the data for spatial distortions inherent to the Anger cameras position response.¹⁹ Using this correction procedure the resolution for the 2D-ACAR can be improved by $\approx 10\%$. All values in the context of the present study stem from uncorrected data as this allows a better assessment of the spectrometer performance.

Variations and drifts in the gain of the electronics cannot be corrected that easily, therefore, in order to damp temperature fluctuations in the experimental hall, the Anger cameras are housed inside acrylic glass boxes.

C. Sample environment

The new 2D-ACAR spectrometer features two interchangeable sample holders, for both heating and cooling the sample. In principle temperatures between ≈ 5 K and 750 K can be achieved depending on the sample and hence enable the study of temperature driven effects on the electronic structure.

The sample holder can be cooled by a closed-cycle cryostat with an extended 22 cm long cold finger. The temperature is controlled with a proportional-integral-derivative controller via two 50 Ω cartridge heaters and a Si diode that are directly coupled to the second stage of the cryostat. Since the temperature at the sample position is slightly different, the sample temperature is separately monitored with an additional temperature sensor which is mounted close to the sample.

The heatable sample holder is composed of a heating filament, which is coiled on a copper rod to increase the inertia of the system. The temperature is measured with a type-K thermo-couple that is fastened to the copper rod and controlled with a standard PI-controller. To minimize the necessary heating power, the heater block is decoupled from the vacuum chamber by stainless steel fittings with low thermal conductivity.

D. Design of the source-sample chamber

The challenges for ACAR lie on the one hand in the maximization of the count rate, and on the other hand in the optimization of the achievable resolution, which is given by the spatial resolution of the detectors, the sample temperature and the positron spot size on the sample. The detector resolution, which is given by the maximum range of the photo-electrons in NaI of 0.62 mm^{20} and the position dependent weighting of the scintillation light by the photomultiplier read-out, cannot be improved easily. Optional sample cooling would reduce the smearing effect of the positron momentum and hence leads to a higher resolution. The resolution smearing due to the positron motion ranges between 0.12 mrad FWHM at low temperatures (< 10 K) and 0.67 mrad FWHM at room temperature.²¹ In order to improve the resolution our main concern is to minimize the positron spot on the sample. In addition, the sample should be easily accessible, and the spectrometer should enable the study of temperature dependent effects on the electronic structure, such as phase transitions.

We took all these considerations into account when designing the setup presented in Figures 1(b) and 1(c). The positrons are emitted from a ^{22}Na source deposited on a Ta reflector inside a standard source capsule, which was developed in the positron group of Martin-Luther-Universität in Halle. The Ta reflector is used to increase the emission of positrons into the lower half-space.

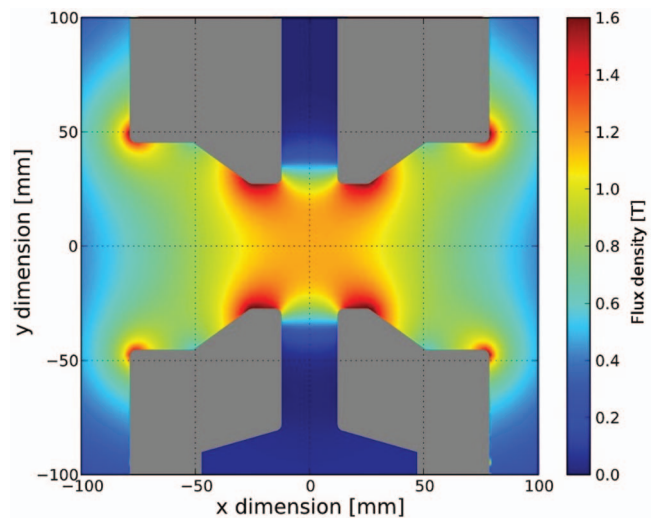


FIG. 2. Magnetic field configuration. FEM simulation of the magnetic flux density inside the sample chamber. Between the two pole pieces a region with a homogeneous field is created. Sample and source are placed inside this region for optimal positron transport.

The source capsule is held inside an elkonite rod, which is connected to a manipulator. The source can be moved into a heavily shielded storage position, for example when the sample is changed. The position of the source capsule and the sample are symmetric with respect to the pole pieces of the electro-magnet. For all considerations presented below a distance between source and sample of 20 mm was chosen, as this value turned out to be optimal with regard to the background produced by the source itself and the positron transport from the source to the sample. A larger distance between source and sample would decrease further the background in the ACAR spectrum, but puts higher requirements to the magnetic guiding field. To produce the guiding field two custom built soft-iron pole pieces are used. The layout of the pole pieces was developed using the FEM physics simulation toolkit COMSOL.²² Diameter and height of the truncated cone shaped pole pieces were optimized in a way that a region with a homogeneous ($< 1\%$ in the direction transverse to the axis between source and sample) flux density is created around sample and source (see Figure 2). The pole pieces have a central bore which allows for the retraction of the source from the sample chamber and for feeding the cold finger of a 4 K closed-cycle cryocooler into the sample chamber. The bore in the base of the lower pole piece is widened so that it can accommodate the heat shield of the cryocooler. The central sample chamber connects the two pole pieces at a fixed distance and also makes them part of the vacuum system. The two pole pieces are therefore an integral part of the sample chamber, which is pumped by a turbo molecular pump from below. This layout frees up space in the central part between the field coils and hence allows the lead shielding to be more compact. The pole piece assembly is placed inside a commercially available electro magnet with a soft iron yoke. A 5 kW high current power supply ($I_{\text{max}} = 75$ A) is used to generate the magnetic field of up to 1.1 T.

The cryocooler is attached to the vacuum system by a differentially pumped rotary platform. This way the orientation

of the sample can be changed by $\pm 90^\circ$ with respect to the detector axis without breaking the vacuum or cooling.

The annihilation radiation produced in the sample leaves the sample chamber through 1 mm thin aluminium windows. The transmission of these windows is 97.7% for 511 keV quanta. In order to screen the background contribution from the source, the sample chamber is enclosed by lead shielding with a 16 mm bore along the line of sight from the sample to the detectors. Therefore, apart from the line of sight of the detectors the radiation exposure in the lab is minimized.

E. Magnetic field configuration

The field configuration was measured with a Hall probe mounted on a 3-axes stepper motor driven manipulator. In this way, the field through the entire sample chamber was mapped out and compared to the FEM simulation shown in Figure 2. Excellent agreement is found concerning the shape of the field distribution. Exemplary a central line scan through the chamber in the sample plane is shown in Figure 3. The plateau is centred around the sample position and has a diameter (at $0.98 \cdot B_{max}$) of 20 mm, which is well above the typical sample diameter of 6–8 mm. The strength of the magnetic stray field drops rapidly outside the magnetic yoke to values < 1 mT at a distance of more than 40 cm.

The maximum achievable flux density is limited by the current through the coils, since the distance of the pole pieces is fixed. Using water cooled copper coils, a flux density of up to 1.2 T can be achieved. However, during routine operation a value of 1.0 T is chosen, as this greatly reduces the heat dissipation in the coils. Also, the soft iron is already beginning to saturate at such high fields (see Figure 4).

III. PERFORMANCE

The overall performance of a 2D-ACAR spectrometer can be judged by two figures of merit: count rate and resolution. In order to minimize statistical uncertainties, typically 10^8 events are collected in each spectrum. Therefore, the measurement time is determined by the achieved count

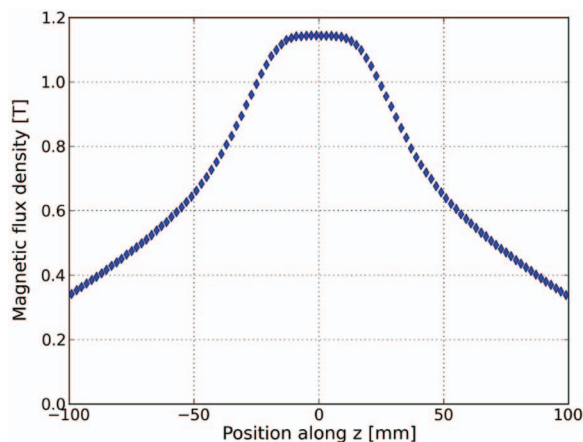


FIG. 3. Magnetic field configuration. Measured magnetic field in sample plane. The sample position is located on the plateau in the center. The flux density decreases rapidly outside the pole piece configuration.

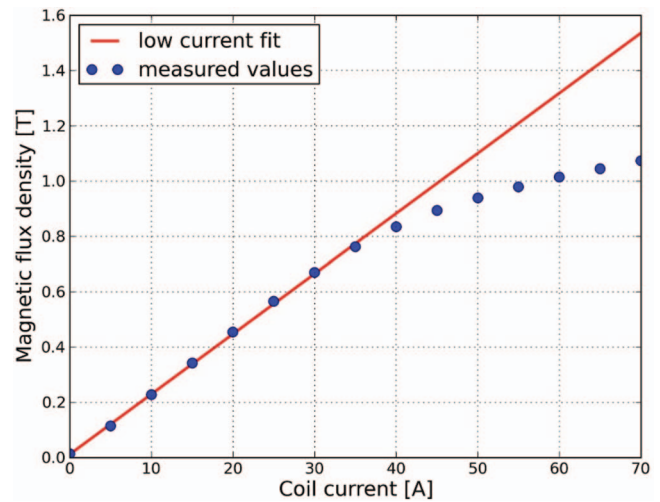


FIG. 4. Dependence of the magnetic flux density at the sample position on the electric current through the coils. At a current of $I_{coil} \approx 45$ A the soft iron is beginning to saturate.

rate, which is correlated to the activity of the source and the positron transport efficiency from the source to the sample. The resolution of the spectrometer is, among other contributions, limited by the spot size on the sample.

A. Positron transport efficiency

The coincident count rate C_r in the detectors is given by the source activity A , the branching ratio B_r for β^+ -decay of the source nuclide, the detector efficiencies ϵ_1 and ϵ_2 , the solid angle Ω , the transmission η for 511 keV γ -radiation, and the positron transport efficiency β :

$$C_r = 2 \cdot A \cdot \beta \cdot B_r \cdot \eta^2 \cdot \epsilon_1 \cdot \epsilon_2 \cdot \Omega / 4\pi.$$

The positron transport efficiency accounts for the probability of a positron produced in the source to hit the sample. For this estimation the deviation from collinearity of the annihilation quanta is not considered, as only the edge region of the detectors is affected. The individual efficiencies of the detectors can be easily determined by the ratio of the individual single count rates and the coincident count rate. The efficiency values are found to be $\epsilon_1 = (7.4 \pm 0.1)\%$ and $\epsilon_2 = (6.6 \pm 0.1)\%$. The source activity at the time of this study was $A = (1.56 \pm 0.05)$ GBq.

The branching ratio for β^+ -decay of ^{22}Na is 90.3%.²³ The factor of 2 has to be considered, as the two annihilation γ rays cannot be distinguished. Also the absorption $1 - \eta = 18.6\%$ of 511 keV quanta in the chamber windows (5 mm in this case) and in the air between the chamber and the detectors has to be taken into account. Finally the solid angle is given by the distance between the detectors and the sample and the active area of the detectors $\Omega = 1.58 \times 10^{-4} \cdot 4\pi$.

For the target a low- Z -material was chosen to minimize the effect of positron reflection, in this case a polycrystalline aluminium disc with a diameter of $d = 10$ mm. With a magnetic flux density of about 1 T a coincident rate of $C_r = 1.0 \times 10^3 \text{ s}^{-1}$ was achieved. Therefore, the positron transport efficiency can be calculated to be $\beta = 69\% \pm 4\%$.

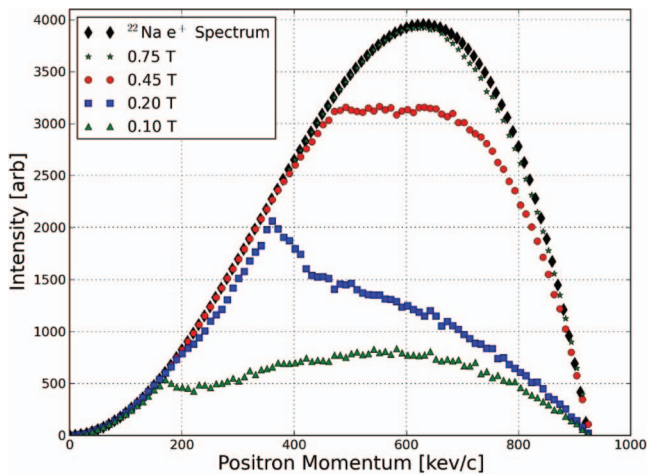


FIG. 5. Calculated positron momentum distribution on the sample, obtained by a Monte-Carlo simulation. For high flux densities almost the full spectrum is mapped onto the sample.

This value, meaning that essentially two of three produced positrons hit the sample, appears surprisingly high, as the positron emission from ^{22}Na is isotropic. Only positrons which are emitted into the lower half space can be guided onto the sample, and self absorption inside the source would lead to a reduced positron yield at the sample.

In order to compare measured positron intensities with calculated ones Monte-Carlo simulations were performed for various magnetic guide fields. The momentum distributions of positrons hitting the sample are shown in Figure 5 together with the full spectrum from the source. In Figure 6, the measured count rate on an aluminium disc with a diameter of $d = 10$ mm is compared with the expected count rate if only emission of positrons into the lower half space is considered. As can be seen, the measured count rate exceeds the expectation for magnetic flux densities higher than 0.1 T. This can be understood in terms of the Ta backing of the source, as this increases the positron emission into the lower half space.

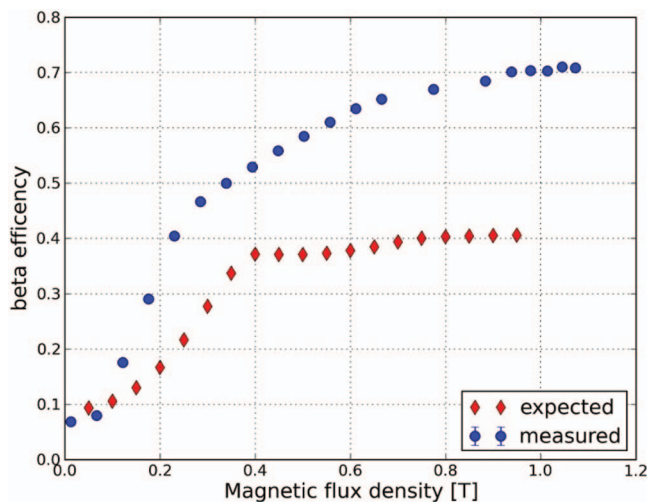


FIG. 6. Measured beta efficiency in comparison with the expectation derived from the simulation. The measured values exceed the expectation indicating that positrons which are emitted into the upper half-space are effectively reflected downwards onto the sample by the Ta reflector.

B. Determination of the positron spot size

The size of the positron spot on the sample has been measured by moving a guillotine-shaped aluminium target sheet, which was mounted on a linear translation stage, through the opened sample chamber. The annihilation radiation was measured with a bismuth-germanate scintillation detector that was collimated to the target. By recording the count rate as a function of the target position the spot profile can be estimated by taking the derivative of the measured integral distribution. In this way two orthogonal cuts through the spot profile could be measured simply by flipping the guillotine-shaped target, without having to change the direction of the translation stage.²⁴

The measurement was performed for different magnetic fields. The cuts are found to have a profile that can be described by a single Gaussian. An absolute error of ± 0.35 mm is assumed for limited positioning accuracy of the translation stage. In combination with the statistical error from the fitting procedure a total error of 0.5 mm appears reasonable. Within the estimated error the values for the FWHM in the two directions are compatible (see Figure 7). The resulting spot diameter (FWHM) at typical operation conditions (1 T) is found to be (5.4 ± 0.5) mm. Hence, the contribution to the angular resolution in x direction is given by (0.65 ± 0.06) mrad FWHM for a sample-detector distance of 8.25 m.

C. First 2D-ACAR measurements

A way to directly determine the total angular resolution is the 2D-ACAR measurement of thermalized positronium.^{25–27} The angular correlation of its annihilation radiation is only influenced by the thermal momentum of the positronium itself.^{28,29} For this study α -quartz is used as a sample material, because it shows significant formation of positronium, which is thermalized inside the crystal lattice. According to the periodicity of the lattice the positronium wavefunction is therefore represented as a delocalized Bloch-state.³⁰ This can be confirmed in the ACAR measurement since in the momentum domain, the higher order momentum components are

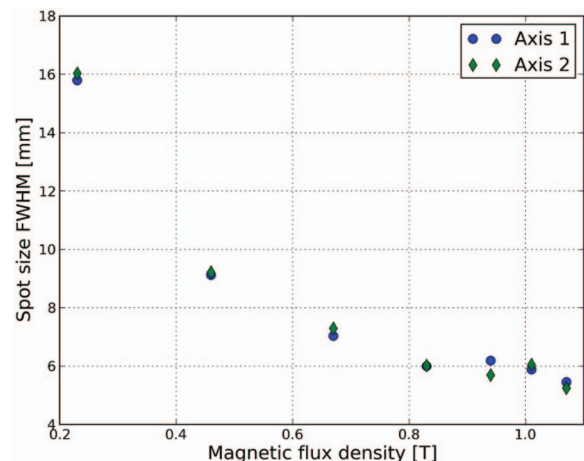
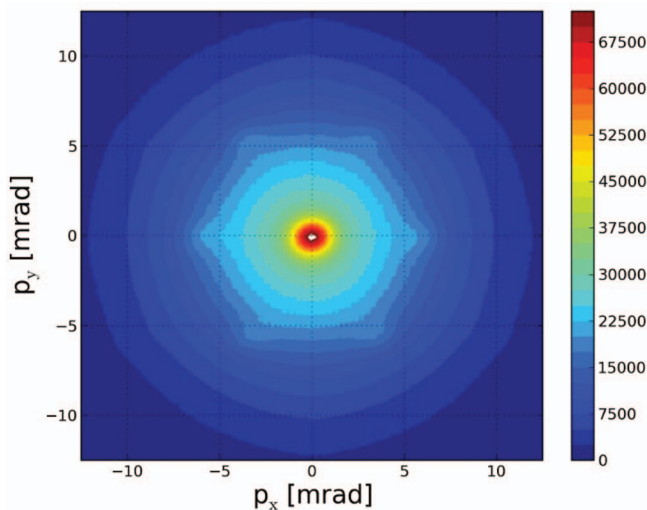


FIG. 7. Dependence of the spot diameter on the magnetic flux density at the sample position for two arbitrary orthogonal axis.

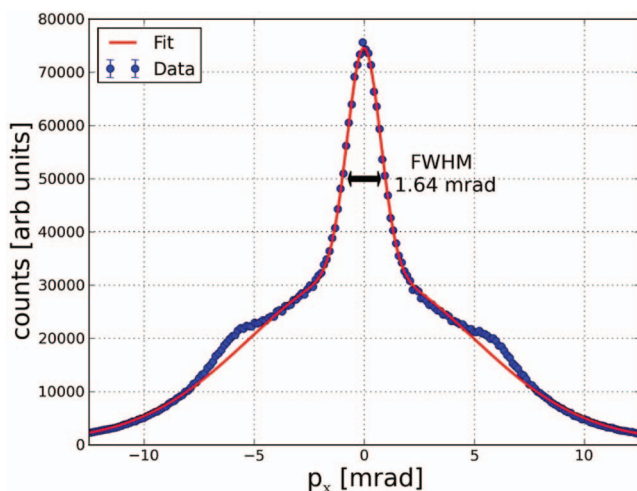
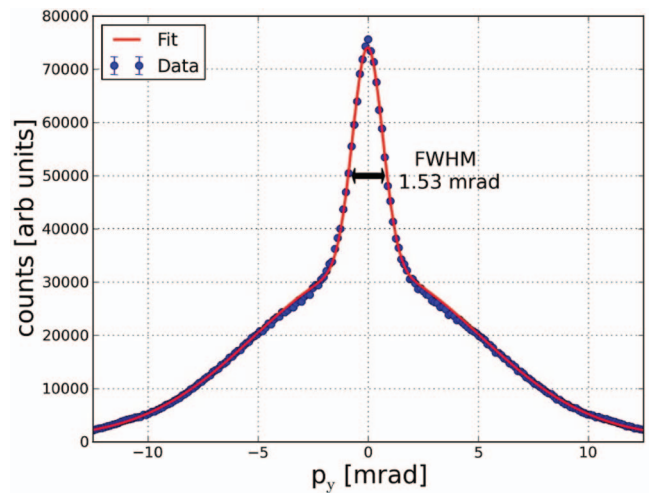
FIG. 8. Contour plot of the ACAR spectrum of single crystalline α -quartz.

observable at the positions of the reciprocal lattice vectors (see Figure 8).

In the cross-sections of the 2D-ACAR spectrum (Figures 9 and 10) two features can be distinguished. The narrow component accounts for the para-positronium signal, while the wide component stems from direct positron annihilation and positronium pick-off annihilation. A superposition of two Gaussians is used to describe the data.

The width of the narrow component is determined by the angular resolution, which is different for horizontal (x) and vertical (y) direction, since the spot size only contributes to the resolution broadening in the x direction (see Fig. 9). The spot size in x direction is given by the lateral distribution of the positrons on the sample, while the lateral extension in the y direction (see Fig. 10) is determined by the implantation depth of the positrons into the sample, which is of the order of $200 \mu\text{m}$ for quartz and therefore can be omitted.

Since all contributions to the angular resolution (thermal smearing, spot size, detector resolution) are independent, the total angular resolution is given by the sum in quadrature over

FIG. 9. Horizontal cut through the ACAR spectrum along $p_y = 0$.FIG. 10. Vertical cut through the ACAR spectrum along $p_x = 0$.

the individual contributions:

$$\sigma_{\text{tot}} = \sqrt{\sigma_{x,y}^2 + \sigma_{\text{det}}^2 + \sigma_{\text{therm}}^2}.$$

A value of $(1.53 \times 1.64) \text{ mrad}^2$ FWHM was achieved at room temperature. Hence, the contribution of the spot size can be extracted, as it is only present in the horizontal component. By taking the values given in Figures 9 and 10 the contribution of the spot size is estimated to be $(0.61 \pm 0.13) \text{ mrad}$ FWHM, which is within the error compatible with the contribution to the resolution that was inferred from the directly measured spot size presented in Sec. III B. The error of this approximation stems from the statistical accuracy of the fitting procedure.

IV. CONCLUSION AND OUTLOOK

A new 2D-ACAR spectrometer has become operational at the Technische Universität München. The above-mentioned design goals concerning count rate and resolution were accomplished. We could prove that the contribution to the overall resolution from the spot size is compatible with the measured spot size and therefore well understood. Hence, the next step, the systematic investigation of the electronic structure of correlated materials and the study of temperature driven effects on the electronic structure can be undertaken. In the near future we plan to move the setup to the new experimental hall of the FRM II and use the mono-energetic positron beam NEutron induced POSitron Source MUniCh (NEPOMUC). This allows us to increase the detector-sample distance and to perform depth-dependent measurements in order to track the evolution of the electronic structure from the surface to the bulk, which will add a new quality to the 2D-ACAR measurements.

ACKNOWLEDGMENTS

This project is funded by the Deutsche Forschungsgesellschaft (DFG) within the Transregional Collaborative Research Center TRR 80 “From electronic correlations to functionality.”

- ¹S. B. Dugdale, H. M. Fretwell, M. A. Alam, G. Kontrym-Sznajd, R. N. West, and S. Badrzadeh, *Phys. Rev. Lett.* **79**, 941 (1997).
- ²H. M. Fretwell, S. B. Dugdale, M. A. Alam, D. C. R. Hedley, A. Rodriguez-Gonzalez, and S. B. Palmer, *Phys. Rev. Lett.* **82**, 3867 (1999).
- ³S. J. Crowe, S. B. Dugdale, Z. Major, M. A. Alam, J. A. Duffy, and S. B. Palmer, *EPL* **65**, 235 (2004).
- ⁴M. Biasini, G. Ferro, G. Kontrym-Sznajd, and A. Czopnik, *Phys. Rev. B* **66**, 075126 (2002).
- ⁵R. J. Hughes, S. B. Dugdale, Z. Major, M. A. Alam, T. Jarlborg, E. Bruno, and B. Ginatempo, *Phys. Rev. B* **69**, 174406 (2004).
- ⁶J. Laverock, S. B. Dugdale, Z. Major, M. A. Alam, N. Ru, I. R. Fisher, G. Santi, and E. Bruno, *Phys. Rev. B* **71**, 085114 (2005).
- ⁷P. Genoud, A. A. Manuel, E. Walker, and M. Peter, *J. Phys.: Condens. Matter* **3**, 4201 (1991).
- ⁸K. E. H. M. Hanssen, P. E. Mijnders, L. P. L. M. Rabou, and K. H. J. Buschow, *Phys. Rev. B* **42**, 1533 (1990).
- ⁹T. D. Haynes, R. J. Watts, J. Laverock, Z. Major, M. A. Alam, J. W. Taylor, J. A. Duffy, and S. B. Dugdale, *New J. Phys.* **14**, 035020 (2012).
- ¹⁰H. Haghighi, J. H. Kaiser, S. Rayner, R. N. West, J. Z. Liu, R. Shelton, R. H. Howell, F. Solal, and M. J. Fluss, *Phys. Rev. Lett.* **67**, 382 (1991).
- ¹¹S. B. Dugdale, M. A. Alam, I. Wilkinson, R. J. Hughes, I. R. Fisher, P. C. Canfield, T. Jarlborg, and G. Santi, *Phys. Rev. Lett.* **83**, 4824 (1999).
- ¹²L. Hoffmann, A. K. Singh, H. Takei, and N. Toyota, *J. Phys. F* **18**, 2605 (1988).
- ¹³Y. Nagai, T. Chiba, Z. Tang, T. Akahane, T. Kanai, M. Hasegawa, M. Takenaka, and E. Kuramoto, *Phys. Rev. Lett.* **87**, 176402 (2001).
- ¹⁴J. Laverock, S. B. Dugdale, M. A. Alam, M. V. Roussanova, J. R. Wensley, J. Kwiatkowska, and N. Shiotani, *Phys. Rev. Lett.* **105**, 236401 (2010).
- ¹⁵S. W. H. Eijt, A. T. van Veen, H. Schut, P. E. Mijnders, A. B. Denison, B. Barbiellini, and A. Bansil, *Nature Mater.* **5**, 23 (2006).
- ¹⁶A. Damascelli, Z. Hussain, and Z.-X. Shen, *Rev. Mod. Phys.* **75**, 473 (2003).
- ¹⁷H. O. Anger and D. H. Davis, *Rev. Sci. Instrum.* **35**, 693 (1964).
- ¹⁸A. C. Kruseman, "Two-dimensional ACAR and low-background DBAR on materials with defects," Ph.D. dissertation (Delft University of Technology, 1999).
- ¹⁹M. Leitner, H. Ceeh, and J.-A. Weber, *New J. Phys.* **14**, 123014 (2012).
- ²⁰M. J. Berger, J. S. Coursey, M. A. Zucker, and J. Chang, "Stopping-Power and Range Tables for Electrons, Protons and Helium Ions," National Institute of Standards and Technology, Gaithersburg, MD, 2005, NISTIR 4999, see <http://physics.nist.gov/Star> (2012/6/15).
- ²¹P. Kubica and A. T. Stewart, *Can. J. Phys.* **61**, 971 (1983).
- ²²*Sealing Technol.* **2010**(7), 4.
- ²³R. Firestone, *Nucl. Data Sheets* **106**, 1 (2005).
- ²⁴C. Hugenschmidt, G. Kögel, R. Repper, K. Schreckenbach, P. Sperr, and W. Triftshäuser, *Nucl. Instrum. Methods Phys. Res. B* **198**, 220 (2002).
- ²⁵R. N. West, J. Mayers, and P. A. Walters, *J. Phys. E* **14**, 478 (1981).
- ²⁶G. Dai, A. Weeber, and P. Mijnders, *Nucl. Instrum. Methods Phys. Res. A* **306**, 261 (1991).
- ²⁷S. Berko, M. Haggoie, and J. Mader, *Phys. Lett. A* **63**, 335 (1977).
- ²⁸H. Ikari, *J. Phys. Soc. Jpn.* **46**, 97 (1979).
- ²⁹P. Kubica and A. T. Stewart, *Phys. Rev. Lett.* **34**, 852 (1975).
- ³⁰A. Greenberger, A. Mills, A. Thompson, and S. Berko, *Phys. Lett. A* **32**, 72 (1970).